Microstructure Integrated Modeling of Multiscan Laser Forming

Jin Cheng

Y. Lawrence Yao

Department of Mechanical Engineering,
Columbia University,
New York, NY 10027

Laser forming of steel is a hot forming process with high heating and cooling rate, during which strain hardening, dynamic recrystallization, and phase transformation take place. Numerical models considering strain rate and temperature effects only usually give unsatisfactory results when applied to multiscan laser forming operations. This is mainly due to the inadequate constitutive models employed to describe the hot flow behavior. In this work, this limitation is overcome by considering the effects of microstructure change on the flow stress in laser forming processes of low carbon steel. The incorporation of such flow stress models with thermal mechanical FEM simulation increases numerical model accuracy in predicting geometry change and mechanical properties.
[DOI: 10.1115/1.1459088]

1 Introduction

Laser forming is a hot working process, during which thermal distortion induced by a laser beam is made use of to shape material without hard tooling or external forces. Numerical and experimental investigations of laser forming processes were carried out to better understand process mechanisms and the effects of key process parameters on dimension and mechanical properties of the formed parts [1,2,3]. Temperature and strain-rate dependent material properties were compiled and considered in the numerical models developed for concave, convex, and tube laser-forming processes, and nonlinear relationships including appropriate flow rule and yield criterion were specified for plastic deformation [4,5,6]. Experimental observations, however, have shown that the laser forming processes of metals are often accompanied by recovery, recrystallization and phase transformation [7,8,9,10]. To enhance modeling accuracy and prediction capability, variations in material properties, such as in flow stress, caused by microstructure changes need to be considered in numerical simulation of the laser forming process.

It is important to consider the microstructure changes in modeling the laser forming process because, first of all, for the high temperature experienced in the process, flow stress is more significantly influenced by the microstructure changes. Secondly, laser forming like other hot working processes, is characterized by work hardening simultaneously relieved by dynamic softening processes. Apart from recovery, dynamic recrystallization is the primary softening mechanism determining the stress-strain relationship of a material and, hence its flow behavior. This is especially true for metals such as steels, which exhibit relatively low stacking fault energy. In particular, the simultaneous hardening and softening process repeats and its effects accumulate in multiscan laser forming, during which repeated heating and deforming take place to achieve the magnitude of deformation required for practical 3-D laser forming.

The fundamental of physical metallurgy of hot working of steel is well established. Various research groups [11,12,13] have developed material models for the mathematical description of recovery and recrystallization behavior based on semi-empirical equations. The incorporation of such models with finite element method (FEM) based simulation to predict local microstructure has led to more accurate results. For instance, Karhausen and Kopp [14] presented a model offering improved implementation of material behavior in plastomechanical simulations of hot-forming processes. The developed model was validated to increase the accuracy in terms of structural description and flow stress determination. Pauskar and Shivpuri [15] considered recovery and dynamic recrystallization in the flow stress model for hot rolling.

Laser forming differs from other hot working processes in that significantly higher heating and cooling rate is involved. This is generally true for processes using a laser beam but laser forming also involves fairly high strain and strain rate. Ashby and Easterling [16] investigated the transformation of steel surface treatment by laser beams. They presented a kinetic model that considers the rapid heating and cooling rate effects on metallurgy of steel. They combined the solutions to the heat flow and the kinetic models to predict the near surface structure and hardness after laser treatment. But the deformation involved is small. Chen et al., [17] considered the austenitization temperature change due to the superheating during laser surface hardening. They applied the transformation temperature change to FEM simulation, and the results showed that considering microstructure dependent physical properties are important. In this paper, the effects of microstructure change on the flow stress in laser forming processes of steels are examined in the context of higher heating and cooling rate. Appropriate models of microstructure changes are incorporated into thermal-mechanical FEM simulation in order to better predict the mechanical properties and geometry change of the formed parts.

2 Microstructure Dependent Flow Stress Modeling for Laser Forming

2.1 Modeling scheme. A typical laser forming process of low carbon steels undergoes the stages listed in Table 1, where A_{1ne} is the nonequilibrium lower transformation (austenitization) temperature, A_{3ne} the nonequilibrium upper transformation temperature, and 700 K is approximately the starting temperature for martensite formation of low carbon steels. Table 1 was obtained by comparison of FEM analysis [10] and Fe-carbon equilibrium phase diagram taking into account non-equilibrium effect. The determination of the nonequilibrium transformation temperature due to superheating will be discussed in Sections 2.4 and 4.1.

The overall strategy is to develop a module on recovery/recrystallization and a module on phase transformation, and to interface them with an existing FEM thermal/mechanical model of laser forming (Fig. 1). The FEM model, which has been reported previously [3,5,10] computes thermal and mechanical variables (e.g., temperature, strain, and strain rate). Given these values, the

Contributed by the Manufacturing Engineering Division for publication in the JOURNAL OF MANUFACTURING SCIENCE AND ENGINEERING. Manuscript received March 2001; Revised September 2001. Associate Editor: K. Stelson.

Copyright © 2002 by ASME

Table 1 Microstructure change in typical laser forming processes of low carbon steel sheets

Temp. (K)	300K~ A_{1ne} temp	A_{1ne} temp ~ A_{3ne} temp	A_{3ne} temp ~ peak temp.	peak temp. ~ 700K	700K ~ 300K
time	~50ms	~10ms	~20ms	~20ms	~200ms
plastic deformation	20~25%	~5%	20~30%	30~40%	10~20%
recovery	yes	yes	yes but less significant	yes but less significant	less likely
recrystallization	less likely	likely	yes	yes	yes
phase transformation	ferrite	ferrite -->austenite	austenite	austenite	austenite--> martensite/others

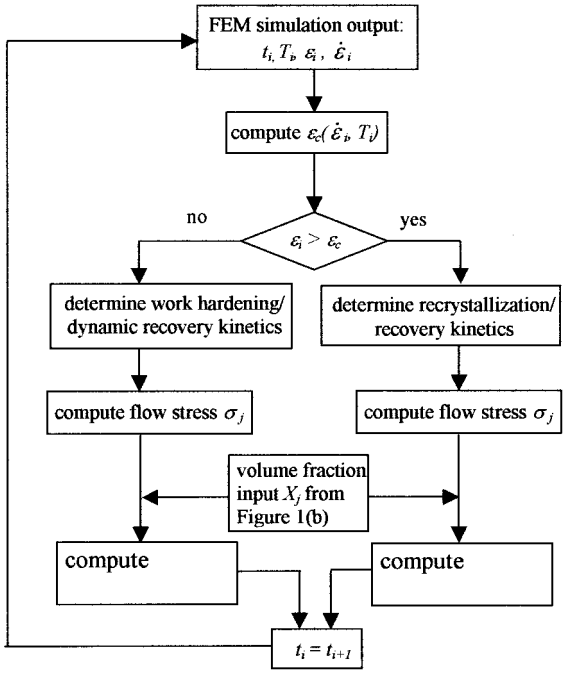

(*a*)

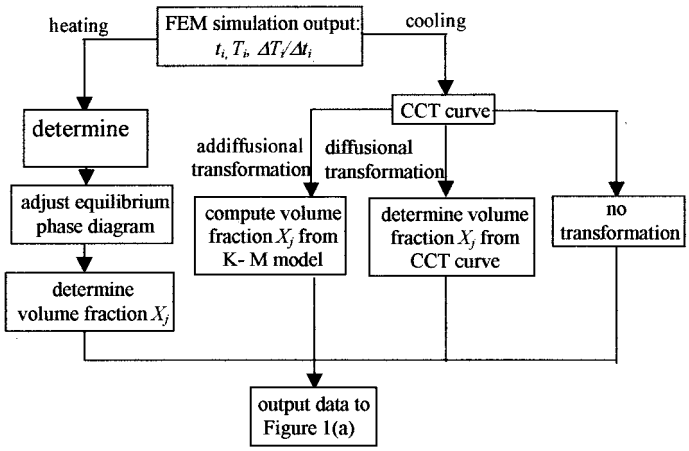

(*b*)

Fig. 1 Algorithm for (*a*) recovery/recrystallization, and (*b*) phase transformation constitutive modeling (index *j* denotes the *j*th phase)

Table 2 Values of the coefficients A, α, Q_{def} and n [20]

	Value	n	α, $m^2 MN^{-1}$	lnA	Q_{def} $kJ.mol^{-1}$
austenite	maximum ($\sigma_{ss}^{\bullet}$)	6.8912	0.0079304	38.355	412
	steady (σ_{ss}^{rex})	6.6422	0.0076101	36.547	387
	initial stress (σ_o)	8.0278	0.01086	49.75	514.8
ferrite	maximum ($\sigma_{ss}^{\bullet}$)	5.76	0.099	34.97	396
	steady (σ_{ss}^{rex})	5.455	0.0994	33.295	374
	initial stress (σ_o)	6.835	0.0135	43.871	474.47

phase transformation module determines volume fractions X_j of different phases depending on whether it is heating or cooling. The austenitization temperature will change due to the high heating rate in laser forming. For a heating stage, an equilibrium phase diagram is adjusted for the high heating rate involved as follows and is used to determine X_j. An experimental method is employed to decide the adjustment in austenitization temperature, as will be discussed in Section 4.1. For a cooling stage, a continuous cooling transformation (CCT) diagram together with semi-empirical models is used to determine X_j (Fig. 1(*b*)). With all these as inputs, the recovery and recrystallization module balances between work hardening and the softening processes of dynamic recovery and dynamic recrystallization, and subsequently determines the flow stress σ by the additive principle (Eq. (1)) of multi phases (Fig. 1(*a*)). Appropriate constitutive relationships used in these modules will be described below.

Isotropic material is considered. It is assumed that no texture will be formed in laser forming induced microstructure change. It is assumed the stress induced by volume change accompanying phase transformations is small and therefore negligible. Grain size effect on flow stress is assumed to be negligible under the conditions used. This assumption is base on the previous observations. Shigenobu et al. [18], and Semuna et al. [19], found that peak strain ε_p of a low carbon steel in torsion can be successfully predicted without considering grain size and its change. Some other studies have removed the grain size term [20] in low carbon steel material models. It is assumed that the material concerned is an aggregated structure of several phases and the contributions of each phase are independent of each other. Therefore, the properties of the multiphase alloy will be a weighted average of the individual phases. In this paper, it is assumed that the phases are subject to equal strain and the material stress is obtained from the weighted average of phase stresses.

$$\sigma = \sum_{j=1}^{N} (X_j \cdot \sigma_j) \tag{1}$$

where σ is the total stress X_j and σ_j are the volume fraction and stress of the jth phase of the material, respectively. It is also assumed that deformation and microstructure induced heat is negligible. The temperature dependence of the material properties such as the modulus of elasticity, thermal expansion coefficient, thermal conductivity, and specific heat follow Bao & Yao [3] and Li & Yao [5].

2.2 Recovery/recrystallization modeling. The algorithm for recovery/recrystallization modeling is schematically illustrated in Fig. 1(*a*). The relationship between the stress-strain curve configuration and corresponding structural event is known from numerous experimental studies covering a broad spectrum of metals. Following the approach of Laasraoui and Jonas [21], the stress strain curve is divided into two regions: the region before the critical strain ε_c where work hardening and dynamic recovery is the predominant mechanism, and the region after the critical strain where dynamic recovery and dynamic recrystallization act together with recrystallization more dominant.

Work hardening and dynamic recovery ($\varepsilon < \varepsilon_c$). The classical approach to modeling the flow stress in this regime consists of the following expression [22], which considers work hardening and dynamic recovery.

$$\sigma^{rec} = [\sigma_{ss}^{*2} + (\sigma_0^2 - \sigma_{ss}^{*2}) e^{-\Omega\varepsilon}]^{0.5} \tag{2}$$

where σ^{rec} represents the flow stress in this regime when dynamic recovery was the only softening mechanism, σ_0 is the initial stress, σ_{ss}^* is the imaged steady state stress when strain is infinite, and Ω represents the ease of dynamic recovery. σ_0, σ_{ss}^*, and Ω in Eq. (2) need to be determined. σ_0 and σ_{ss}^* are determined by the modified hyperbolic sine law [13] given T and $\dot{\varepsilon}$ values from the FEM model:

$$\dot{\varepsilon} = A \exp\left(\frac{-Q_{def}}{RT}\right) \sinh(\sigma\alpha)^n \tag{3}$$

where A, α, Q_{def} and n are material dependent coefficients and are determined as follows [20]. A series of hot forming processes was conducted under different strain rate $\dot{\varepsilon}$ and temperature T to obtain their stress/strain curves. σ_0 and σ_{ss}^* were measured from these curves. All σ_0 (or σ_{ss}^*) values along with $\dot{\varepsilon}$ and T values were substituted into Eq. (3) to determined A, α, Q_{def} and n in a two-step process similar to regression. α and n were first obtained by plotting $\log_{10}(\sigma)$ versus $\log_{10}(\dot{\varepsilon})$ assuming high temperature and (σ) versus $\log_{10}(\dot{\varepsilon})$ assuming low temperature. The values of A and Q_{def} were then be found by plotting $\ln[\dot{\varepsilon}(\sinh(a\sigma)^{-n}]$ versus $1/T$. For AISI 1012 steel used in this paper, values of these coefficients reported by Anderson and Evans [20] are listed in Table 2. As seen, they were determined for two temperature regions, that is, the high one corresponding to austenite and low one corresponding to ferrite region. In each region, the coefficients were determined for σ_0, and σ_{ss}^* (to be used in Eq. (2)) and σ_{ss}^{rex} (to be used in Eq. (6) below).

It should be pointed out that, while the temperature and strain rate obtained from the FEM model are transient, using Eq. (3) assumes quasi-steady state and leads to a level of approximation. Laser forming is a transient process but strain and strain rate involved are less than that in other forming processes. In addition, the time step in the FEM model automatically adapts to temperature and strain rates and gradients. As a result, it is reasonable to tolerate the quasi-steady state assumption associated with Eq. (3). As to the level of approximation, few literatures have reported its estimate. Blum [23] studied modeling of steady state and transient deformation under elevated temperature. He suggested that the form of Eq. (3) is still valid for transient deformation but σ may be modified by a coefficient $k_f > 1$ to account for the transiency.

Ω in Eq. (2) is expressed in form of

$$\Omega = K \cdot \dot{\varepsilon}^{n_1} d_0^{n_2} \exp\left(\frac{-Q}{Rt}\right) \tag{4}$$

where K, n_1, n_2, and Q are material constants. Values of these constants for AISI 1012 steel are adopted from Anderson and Evans [20] and they are $K = 32.5$, $n_1 = 0.055$, $n_2 = 0$, and $Q = 19{,}800$ J/mol. Since the effect of grain size is assumed negligible, n_2 is taken to be zero.

Recrystallization ($\varepsilon > \varepsilon_c$). The fraction of completeness of recrystallization is represented by

$$X_d = \frac{\sigma^{\mathrm{rec}} - \sigma}{\sigma_{ss}^* - \sigma_{ss}^{rex}} = \left[1 - \exp\left(-K_d \left(\frac{\varepsilon - \varepsilon_c}{\varepsilon_{0.5} - \varepsilon_c} \right)^{n_3} \right) \right] \tag{5}$$

which is arranged to obtain flow stress

$$\sigma = \sigma^{rec} - [\sigma_{ss}^* - \sigma_{ss}^{rex}] * \left[1 - \exp\left(-K_d \left(\frac{\varepsilon - \varepsilon_c}{\varepsilon_{0.5} - \varepsilon_c} \right)^{n_3} \right) \right] \tag{6}$$

where σ_{ss}^{rex} represents the steady state stress after recrystallization has progressed through the material. σ_{ss}^{rex} is determined in the same manner as σ_0 and σ_{ss}^* using Eq. (3) and the value is listed in Table 2. Equations (5) and (6) also incorporate work hardening and recovery effects embedded in σ^{rec} and σ_{ss}^*. K_d is 0.693 for most steels, and n_3 is 2 for very low carbon steels (0.11 percent to 0.17 percent) according to Shigenobu et al. [18]. $\varepsilon_{0.5}$ is the strain corresponding to 50 percent softening due to dynamic recrystallization and is determined in that same way as ε_p through Eq. (8). Laasraoui and Jonas [21] derived the critical strain ε_c and strain at peak stress ε_p as follows

$$\varepsilon_c = 0.83 \varepsilon_p \tag{7}$$

$$\varepsilon_p = B \dot{\varepsilon}^{q_1} d_0^{q_2} \exp\left(\frac{Q'}{RT} \right) \tag{8}$$

where B, q_1, q_2, *and* Q' are material constants. As discussed early, the grain size term is neglected and hence q_2 equals to zero. The other constants are determined for AISI 1012 steel based on the experimental data by Anderson and Evans [20] by the least square method. The values for all the coefficients to determine σ_{ss}^{rex} is listed in Table 1. The coefficients used to calculate ε_p are $B = 1.2 \times 10^{-3}$, $q_1 = 0.11$, $q_2 = 0$, and $Q' = 18{,}812$ J/mol. The values of the coefficients to calculate $\varepsilon_{0.5}$ are $B = 6.95 \times 10^{-5}$, $q_1 = 0.035$, $q_2 = 0$, and $Q' = 58{,}454$ J/mol.

2.3 Phase Transformation Constitutive Modeling. Two kinds of phase transformation are considered in the model. The first is allotropic transformation of which the kinetics is controlled by nucleation and growth mechanisms. The second is diffusionless transformations such as martensitic transformations that are considered to be independent of time.

For allotropic transformation, the amount of transformed product (in terms of volume fraction) is generally known to increase exponentially with the kth power of time, and the rate of increase also relates to the diffusion coefficient of the material. An example is the Johnson-Mehi-Avrami equation. Both k and the diffusion coefficient are functions of temperature, and represent the nucleation and growth rates, conditions of nucleation and the geometry of the growing phase. They need to be experimentally determined for a given material and thermal history. In this paper, an approach involving the use of continuous cooling transformation (CCT) diagrams is applied (Section 4.1). The time history of cooling in laser forming determined by the FEM simulation is superposed on a CCT diagram of the same material. The volume fraction is evaluated by identifying the transformation start and finish times for the various phases at different temperatures and using interpolation for intermediate values. Section 4.1, however, shows that diffusionless transformations dominate due to the high cooling rates experienced in laser forming.

For diffusionless transformations, K-M model [24] gives the volume fraction of martensite as a function of temperature:

$$X_{martensite} = X_{parent}(t_0) \cdot (1 - \exp(-K_{M_1}(M_s - T))) \tag{9}$$

with $X_{parent}(t_0)$ the volume fraction of the parent phase at the start of the martensitic transformation and is one for laser forming; M_s the martensite start temperature, which depends on carbon content and is about 748 K for AISI 1012 steel; K_{MI} a material constant, which was experimentally determined to be 0.011/K for steels [24]. The martensite of AISI 1012 steel is comparable to Bainite and Widmanstatten ferrite because of its low a/c ratio. To predict martensite hardness, the cooling rate at M_s for the area of interest calculated by the FEM model is compared with the Jominy hardenability curves [25]. This approach follows Mazumder [26]. The Jominy hardenability curves consider composition, temperature, and cooling rate effects. The algorithm for phase transformation constitutive modeling is schematically illustrated in Fig. 1(b).

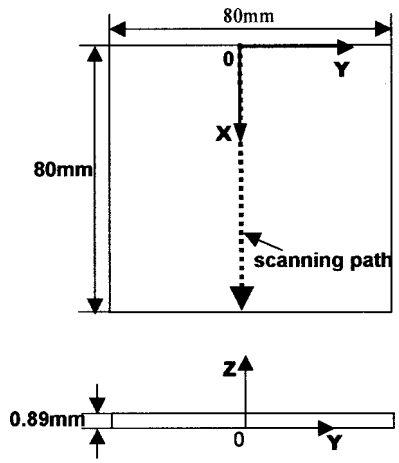

Fig. 2 Geometry of workpiece and coordinate system

2.4 Superheating. For rapid heating, as observed in laser forming, it is important to consider the kinetics of transformation in order to obtain more accurate simulation results. Studies [27] have shown that, for nonequilibrium heating, an additional transformation resistance, i.e., the thermal effect resistance, exists. This resistance increases the transformation temperature so that this additional transformation resistance can be overcome, i.e., a greater transformation driving force has to be attained. For this paper, an experimental method is employed, as will be discussed in Section 4.1, to determine the nonequilibrium transformation temperatures under different process conditions. For example, it was found that the nonequilibrium lower transformation (austenitization) temperature is about 1,033 K and 1,088 K (as opposed to the equilibrium value of 1,000 K) under the two conditions examined (Laser power $P = 400$ W and scanning velocity $V = 25$ mm/s, and $P = 400$ W and $V = 25$ mm/s, respectively). Under both conditions, the heating rate is in the order of 10^4 K/s as determined in the FEM model. These transformation temperature values are adopted in the simulation.

3 Experiment and Simulation Conditions

The straight-line laser-forming scheme with natural cooling is shown in Fig. 2. The scanning path is along the x-axis and the direction perpendicular to the scanning path within the plate is defined as y-axis. To reduce the edge effect [3], scanning is performed back and forth along the x-axis. The material is low carbon steel, AISI 1012, and 80 mm by 80 mm by 0.89 mm in size. To enhance laser absorption by the workpiece, graphite coating is applied to the surface exposed to the laser. Most experiments use either laser power of 400 W and scanning velocity of 25 mm/s or 800 W and 50 mm/s. One experiment involves velocity varying between 25 and 80 mm/s, and other experiments involve power varying between 400 and 800 W. There is no melting involved in laser forming under the conditions in this paper. The exact experimental conditions are noted in the figures and their legends. The experiments were repeated at least three times and the standard deviations of the measured values are indicated by means of error

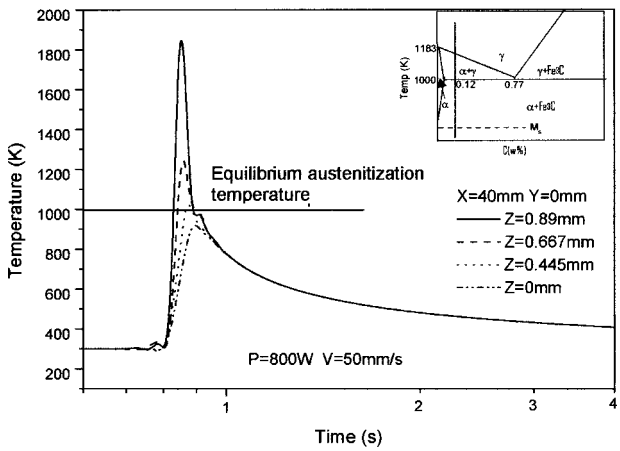

Fig. 3 Typical temperature history of points on the scanning path along the thickness direction from FEM results (AISI 1012 steel)

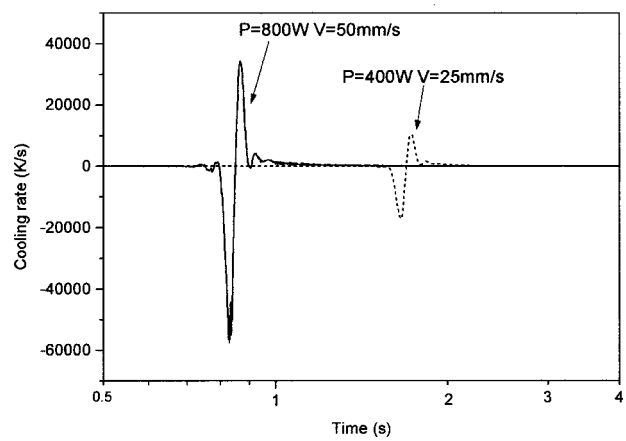

Fig. 4 Typical heating and cooling rate on the top surface along the scanning path ($X=40$ mm, and $Y=0$ mm, and $Z=0.89$ mm) from FEM results. Note: positive value as cooling rate, and negative values as heating rate

bars in figures. The laser system used is a 1500 W CO_2 laser. The laser beam diameter impinging on the workpiece is 4 mm. A coordinate-measuring machine (CMM) is used to measure the bending angle of the formed parts. Scanning electron microscopy (SEM) is used to assist in the determination of the nonequilibrium transformation temperatures and to examine the resultant microstructure changes. Tensile test samples are machined by CNC along the scanning path and tensile tests are conducted on a MTS.

A commercial FEM code, ABAQUS, is used to solve the heat transfer and structural problem similar to what has been reported in Cheng and Yao [10]. The modules on recovery/recrystallization and phase transformation were implemented through ABAQUS subroutines. Fig. 1 shows flowcharts of the microstructure dependent flow stress modeling. Since the heat transfer and deformation are symmetric about the vertical plane containing the scanning path, only half of the plate is modeled in the numerical simulation. The symmetric plane is assumed to be adiabatic. The same mesh model is used for the heat transfer analysis and structural analysis. Two adjacent points in the middle of the symmetric plane are fixed in order to remove the rigid body motion. All other points within the symmetric plane are assumed to move only within the symmetric plane throughout the deformation process. In structural analysis, the twenty-node element has no shear locking, no hourglass effect, and is thus suitable for a bending-deformation-dominated process such as laser forming. In order to remain compatible with the structural analysis, the same twenty-node element is used in heat transfer analysis. The boundary conditions used include that the top surface is cooled by a weak gas flow. The remaining surfaces are cooled through free convection with atmosphere. Surface heat flux follows $q=q(\underline{x},t)$, surface convection $q=h(T-T^o)$, where $h=h(\underline{x},t)$ is the film coefficient, and $T^o=T^o(\underline{x},t)$ the surrounding temperature, and radiation $q=A((T-T^z)^4-(T^o-T^z)^4)$, where A is the radiation constant and T^z the absolute zero on the temperature scale used. A user-defined FORTRAN program was necessary to model the heat source input from the Gaussian laser beam.

4 Results and Discussions

4.1 Preparatory experiments and simulation. Figure 1 shows laser-scanning path in relation to the workpiece and the coordinate system. Figure 3 shows a typical time history of several points along the thickness direction during laser forming obtained from the FEM model. Part of the iron-carbon equilibrium phase diagram is also shown in the figure as an approximate guide to transformation temperatures for AISI 1012. As seen, the point on the top surface ($Z=0.89$ mm) experiences temperature much higher than the transformation temperatures while the one near the bottom surface ($Z=0.0$ mm) a much lower temperature.

Superheating. Figure 4 shows typical heating and cooling rates experienced by points near the top surface of the workpiece along the scanning path obtained from the FEM model. As seen, the magnitude of heating rate reaches about 5.5×10^4 K/s (represented by a negative value). To determine the nonequilibrium transformation temperatures, an experimental method with the aid of the FEM model is used and explained as follows. Figure 5 shows the SEM images of the cross section perpendicular to the scanning path after laser forming under two conditions. A distinctively darkened region is observed below the top surface under both conditions. As it will be shown in Fig. 8, the darkened region clearly underwent phase transformation during the laser forming process. No melting was involved. The larger extent of the region under the condition of $P=800$ W, $V=50$ mm/s is attributed to the higher temperature the material experienced than that under the other condition. Figure 6 shows the isothermal contours by the FEM analysis under the same two conditions. Comparison of the location of the darkened region boundary shown in Fig. 5 and the temperature contours at the corresponding location shown in Fig. 6 leads to the determination of the nonequilibrium lower transformation temperature A_{1ne} as 1,088 K and 1,032 K (indicated by the dotted lines in Fig. 6) for the two conditions, respectively. The more significant superheating under the condition of $P=800$ W, $V=50$ mm/s is obviously due to the higher heating rate involved (Fig. 4). These values are then used in the computer modeling of phase transformation by adjusting the austenitization point up from equilibrium austenitization temperature to account for the effect of superheating. The rationale of the approach is based on a simple fact that only points experienced temperature above the lower transformation temperature during heating may experience phase transformation during subsequent cooling.

Undercooling. Figure 7 shows the superposition of cooling curves of laser forming from FEM results on the continuous cooling transformation (CCT) diagram of AISI 1012 steel. As seen, the high cooling rates experienced by both the points near the top surface and the bottom surface precludes significant diffusion controlled phase transformations. The points near the top surface primarily transformed to martensite. This is also evident in Fig. 8(a), which shows a magnified view of the darkened region shown in Fig. 5(b). The structure seen is in the form of lath martensite consisting of parallel arrays or stacks of board- or lath-shaped crystals. This lath martensite produced by high cooling rate consists of high densities of tangled dislocations, reflecting lattice

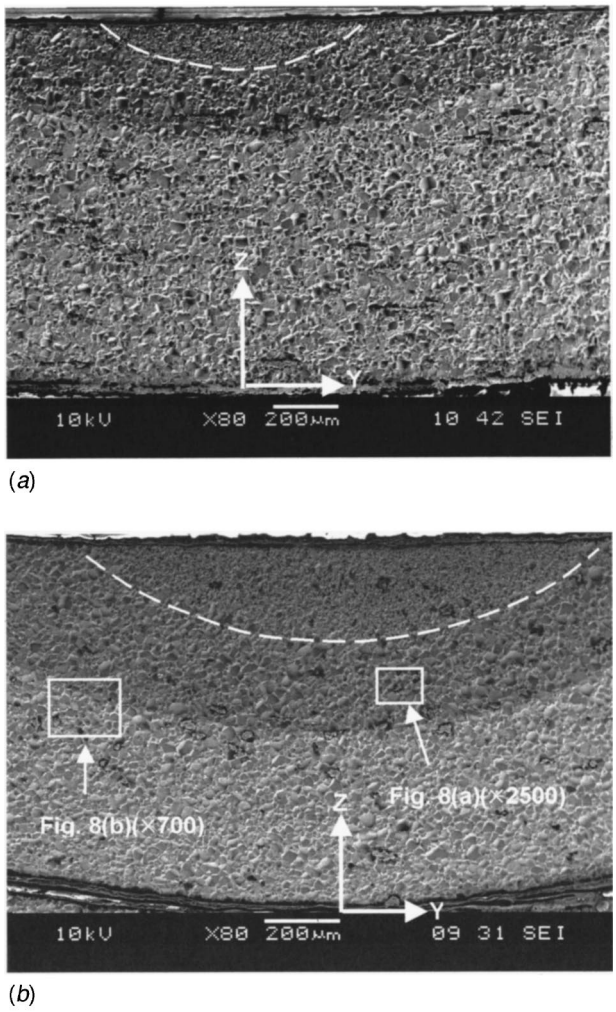

Fig. 5 SEM micrographs of the cross section perpendicular to the scanning path, showing the hardened (dark-colored, no melting involved) zone below the laser scanned top surface of AISI 1012 steel under the conditions of (*a*) *P*=400 W, *V* =25 mm/s and (*b*) *P*=800 W, *V*=50 mm/s (grain refinement is seen in the region surrounded by dashed lines)

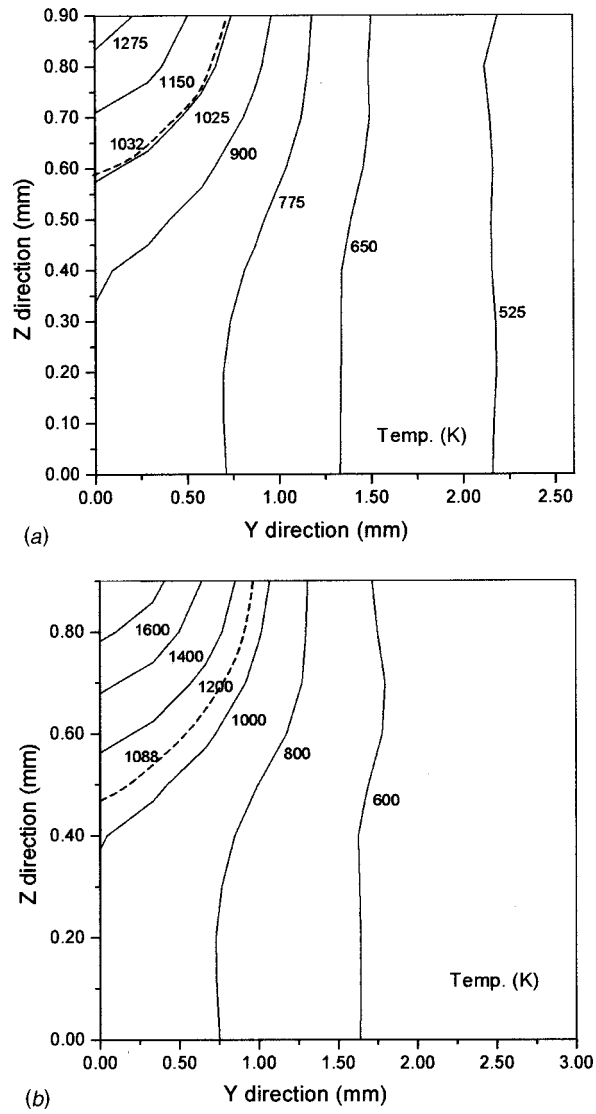

Fig. 6 Isothermal temperature contours from FEM results on the cross section normal to the scanning direction when laser is scanning under the conditions of (*a*) *P*=400 W, *V* =25 mm/s, and (*b*) *P*=800 W, *V*=50 mm/s (half of the cross section is simulated due to symmetry). The dotted lines the extent of the darkened areas in Fig. 5 and are used as the non-equilibrium lower transformation temperature A_{1ne}. No melting is involved.

invariant deformation and volume accommodation effects during athermal transformation from high temperatures. The points near the bottom surface, although also experienced a high cooling rate, did not experience phase transformation since they were not heated even above the equilibrium transformation temperature (Fig. 7). Figure 8(b) shows a magnified view of the boundary between the darkened region and nondarkened region. As seen, the darkened region consists mainly of martensite, while the non-darkened region mainly ferrite and a very small amount of pearlite, which is typical maiden microstructure of low carbon steels like AISI 1012 used in this study. In summary, AISI 1012 steel mainly underwent martensite transformation or no phase transformation in laser forming because the high cooling rate experienced by every points including the ones near the bottom surface prevents diffusion-controlled phase transformations from taking place in a significant fashion.

Dynamic Recrystallization Extent. As seen in Fig. 5, there is a sub-region (surrounded by dashed lines) immediately below the top surface within the darkened zone, where the grains are visibly refined. This is indicative of the significant dynamic recrystallization that took place along with plastic deformation and phase transformation because this sub-region experienced the highest temperature rise and fall and the greatest plastic deformation as well. This also provides experimental evidences for the recrystallization modeling used in simulation. For example, the *y*-axis extent of the grain-refined zone on the top surface is about 0.98 mm and 1.26 mm under the conditions of P=400 W, V=25 mm/s and P=800 W, V=50 mm/s, respectively. This *y*-axis extent of 1.26 mm is drawn on the *y*-axis plastic strain curve shown in Fig. 9, in which peak temperature experienced on the top surface is also superposed. Since dynamic recrystallization occurs only when a critical strain is reached and when temperature is elevated, one can state based on Fig. 9 that when the *y*-axis plastic strain exceeds approximately 1.33 percent and the temperature is approximately above 1,400 K, dynamic recrystallization is significant. Note that this statement is valid because the *y*-axis plastic strain is typically several orders of magnitude higher than the plastic strains along other directions as shown from the FEM model.

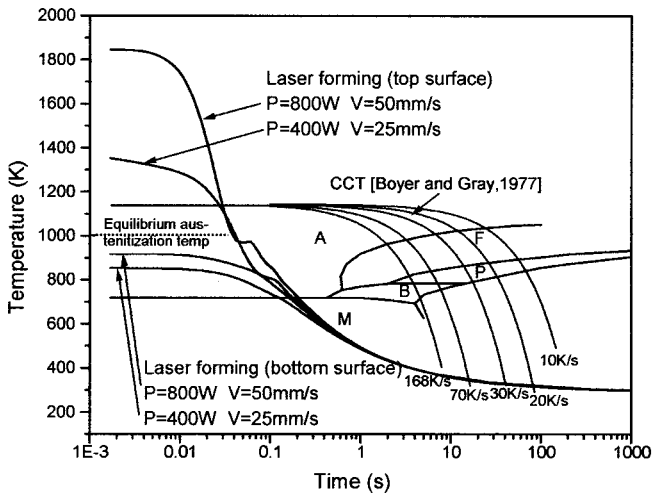

Fig. 7 Superposition of cooling time history of laser forming from FEM results on CCT curve of AISI 1012 steel [28]

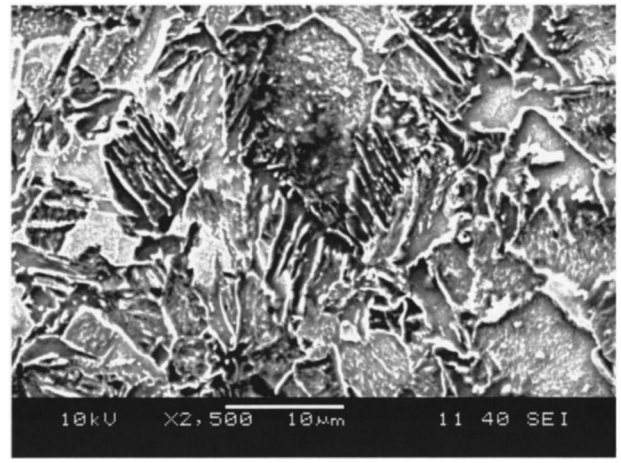

(*a*)

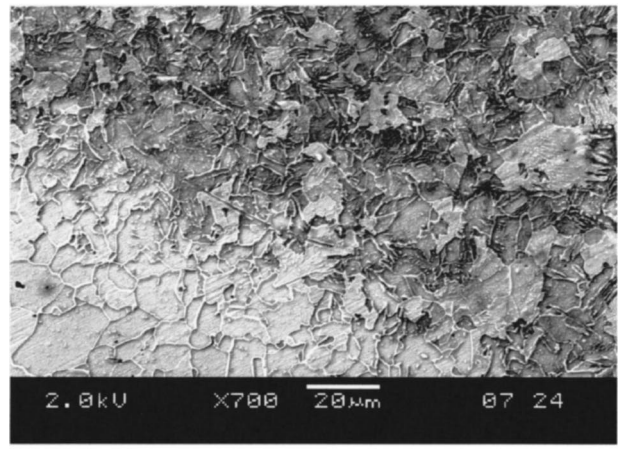

(*b*)

Fig. 8 Detailed SEM micrographs of AISI 1012 steel after laser forming under the condition of $P=800$ W, and $V=50$ mm/s (*a*) primarily martensite structure within the hardened zone (x2500) and (*b*) microstructure around the boundary between the hardened (dark colored) and untransformed (light colored) zone (x700) (also see Fig. 5)

4.2 Prediction of Geometry Change with Microstructure Consideration

Multiscan. Figure 10 shows the comparison of experimentally measured bending angles with simulation results based on models with and without microstructure consideration for a 10-scan laser forming process under two conditions ($P=800$ W, $V=50$ mm/s, and $P=400$ W, $V=25$ mm/s). The scans were carried out along the same scanning path with alternate directions in order to reduce the edge effect. Enough time was allowed between scans in both experiments and simulation in order for material to cool down near the room temperature. In practice, forced cooling is normally used to speed up the multiscan process [10]. The model without microstructure changes considers only the effects of temperature, strain rate and work hardening on flow stress, while the model with microstructure change considers softening mechanisms of dynamic recovery and recrystallization, as well as the effect of phase transformation on the flow stress, in addition to the effects already considered above. The details of the model with microstructure change are discussed in Section 2.

It is seen from Fig. 10 that there is not much difference between the predicated angles by the two models for the first scan. However, with increasing number of scans, the difference widens. The bending angle predicted by the model with microstructure consideration matches experimental measurements better. The model without microstructure consideration underestimates the flow stress and thus overestimates the bending angle. More revealing is that the softening effects due to recovery and recrystallization are out-weighted by the hardening effects due to martensite transformation near the top surface. The net effect of microstructure change in laser forming of steels, therefore, is hardening and thus increase of the flow stress. This is consistent with what will be discussed in Section 4.3. Another observation is that the discrepancy between the models with and without microstructure consideration is larger under the condition of $P=800$ W and $V=50$ mm/s than that under the other condition. This is primarily due to the much higher cooling rate experienced under the former condition (Fig. 4), which favors more martensite transformation and thus makes the net effect of hardening greater as compared with that under the other condition. More detailed analysis follows in the next paragraph in which the first two scans are closely examined. The steady-state bending angle values predicted by the models with and without microstructure consideration shown in Fig. 10 are extracted and compared with experimental results in Fig. 11 for greater clarity.

First Scans. The first two scans shown in Fig. 10 are magnified in Fig. 12 for more detailed analysis. It is seen that under the condition of $P=800$ W and $V=50$ mm/s, the hardening effect due to martensite transformation was not as significant as the softening effect due to dynamic recovery and recrystallization in the first scan but quickly surpassed the latter in the second scan. Contrary to that, the net hardening effect under the condition of $P=400$ W and $V=25$ mm/s accumulated in a more graduate fashion. This is because that martensite did not exit at the beginning of the first scan but already exited at the beginning of the second and subsequent scans. This made the softening effect due to dynamic recovery/recrystallization more dominant in the first scan, especially under the condition of $P=800$ W and $V=50$ mm/s where the recrystallization zone was larger, the recrystallization more complete, and the hardened zone larger too (Fig. 5(b)). As a result, the model without microstructure consideration even slightly underestimated the bending angle in the first scan under this condition. Under the condition of $P=400$ W and $V=25$ mm/s, both the hardened and recrystallization zones were smaller (Fig. 5(a)), and thus the absence of martensite at the beginning of the first scan did not make the net hardening effect in the first scan much different from that in the subsequent scans. As a result, the model without

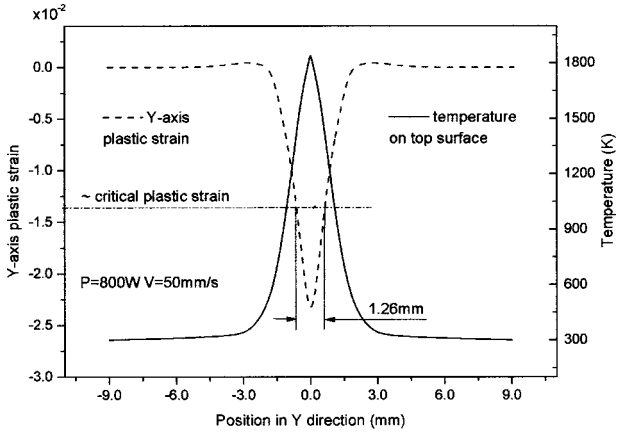

Fig. 9 Y-axis plastic strain and peak temperature (both on the laser scanned top surface) with the Y-axis extent of the grain refined zone (Fig. 5(*b*)) of 1.26 mm to estimate the critical plastic strain

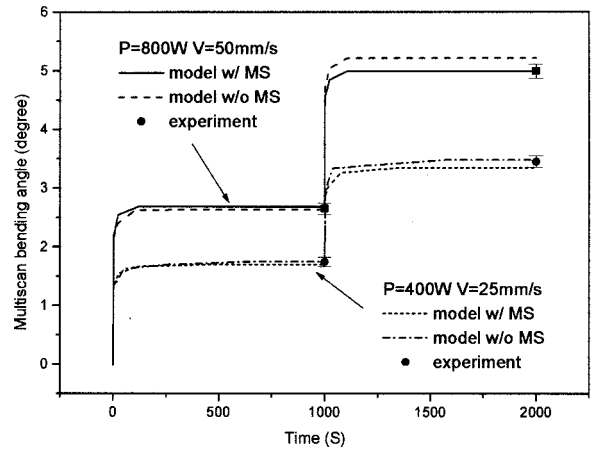

Fig. 12 Detailed view of the first two scans from Fig. 10 (MS-microstructure consideration)

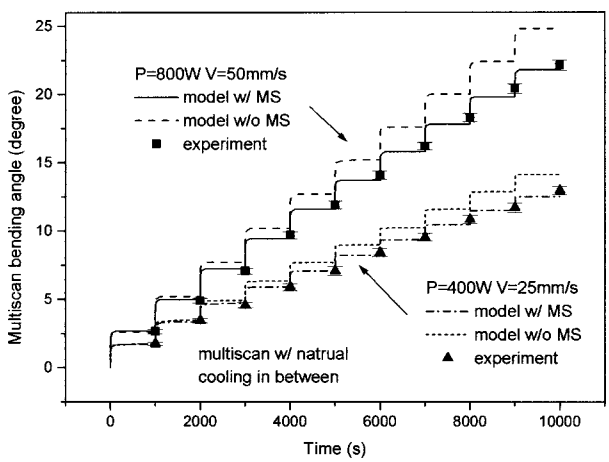

Fig. 10 Comparison of numerical bending angle history *w/* and *w/o* microstructure consideration (MS) with experimental measurements in 10-scan laser forming. Note: FEM computes 1000s for each scan including cooling.

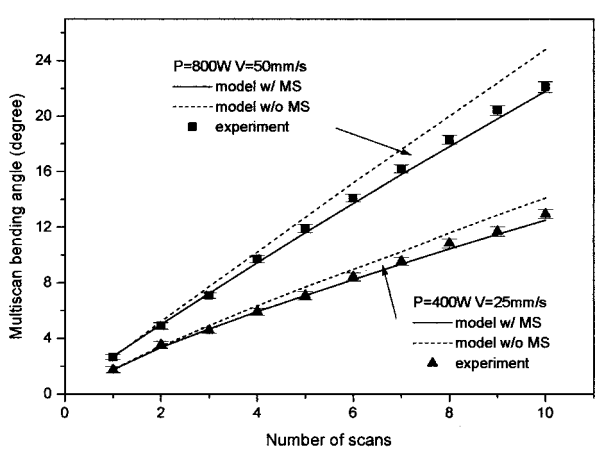

Fig. 11 Comparison of experimental multiscan bending angle with numerical results w/ and w/o microstructure consideration (MS)

microstructure consideration slightly overestimated the bending angle in the first scan under this condition and the overestimate increased moderately in the second scan.

Parametric Sudies. Fig. 13 compares numerical results of the two models with experimental measurements under a wide range of conditions for a single scan. The experimental results agree with the one with microstructure consideration better. As seen, the

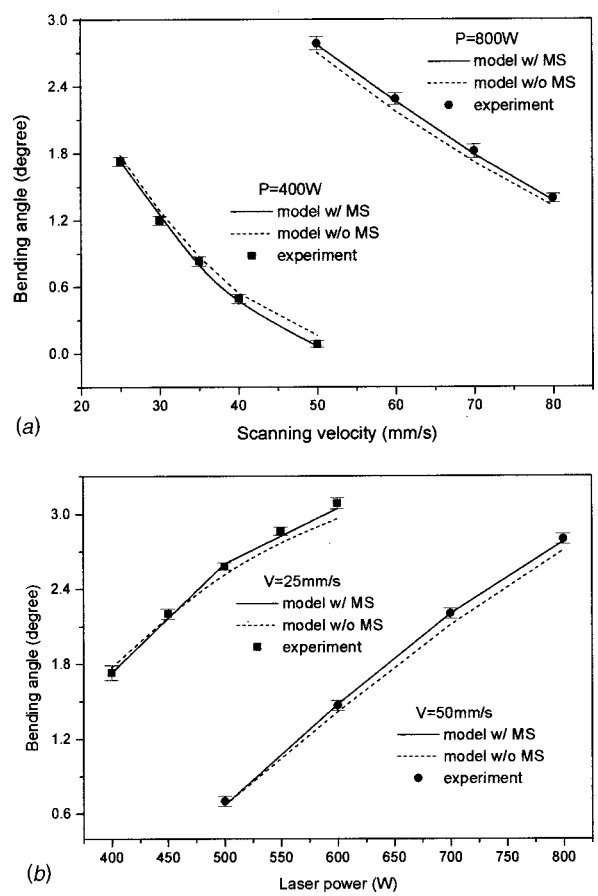

Fig. 13 Parametric studies of single scan bending angle (experimental and numerical results w/ and w/o microstructure consideration (MS)) (*a*) vs. scanning velocity, and (*b*) vs. laser power

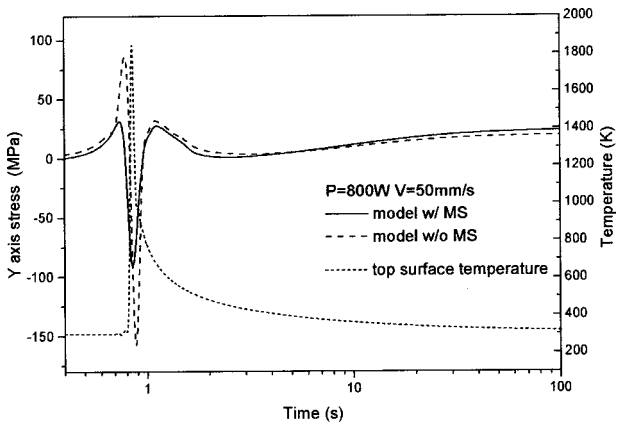

Fig. 14 Comparison of numerical results of *Y*-axis stress history w/ and w/o microstructure consideration (MS)

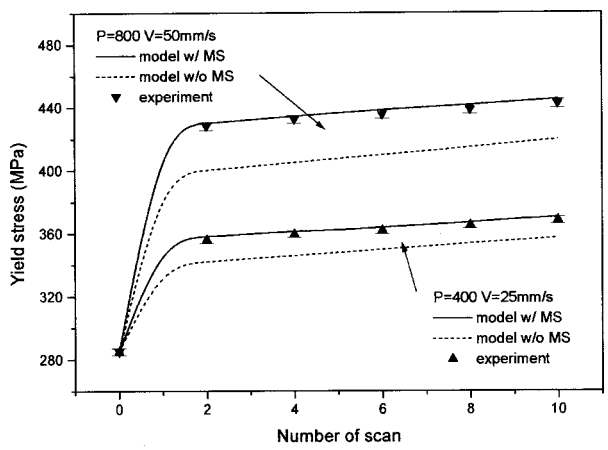

Fig. 15 Comparison of yield stress from numerical modeling w/ and w/o microstructure consideration (MS) with experimental yield stress measurements (samples are scanned for 2, 4,..., 10 times, respectively)

difference between the predicted values by the two models is not great for single scan forming processes. In general, the bending angle with microstructure consideration is slightly smaller than that without microstructure consideration at laser power of 400 W, while the bending angle with microstructure consideration is slightly larger than that without microstructure consideration at high laser power levels. The reason for that has been explained in the last paragraph.

4.3 Effect of Microstructure Consideration on Mechanical Property Prediction. Figure 14 shows a typical *y*-axis stress history experienced by a point on the top surface along the scanning path in a single scan laser forming process as predicted by the two models. The pattern of being tensile first and then significantly compressive before returning to slightly tensile has been well understood and explained in great details in previous literatures [4,5]. It is pointed out here that the stress with microstructure consideration shoots significantly less in both tensile and compressive directions than that without microstructure consideration. This is because the model with microstructure consideration takes dynamic recrystallization into account, which has a softening effect. When the laser beam passes the point and the material starts cooling down, the model with microstructure consideration takes into account the material transformation into martensite. As a result, the compressive stress reverses its direction at about −100 MPa as opposed to about −150 MPa predicted by the model without microstructure consideration. Figure 15 compares the yield stress measured from experiment with the prediction from modeling result with and without microstructure consideration. The details about tensile test specimen can be found in Cheng and Yao [10]. The first sample was scanned twice and its hardness measured. The next (different) sample was scanned four times and its hardness measured. The process repeated until the last sample was scanned ten times and measured. The experimental results agree with the one with microstructure consideration better. This further demonstrates why the model with microstructure consideration can predict the bending angle better.

5 Conclusion

A fundamentally based and empirically calibrated flow stress model for the laser forming process of a low carbon steel has been presented in this article. The effects of strain hardening, dynamic recovery and recrystallization, superheating, and phase transformation have been considered. Application of the present model in the prediction of geometry and mechanical properties in multiscan laser forming has demonstrated significant improvement in accuracy over the model without microstructure considerations. Incorporated with FEM, the present model serves as an enabler for the analysis and design of practical three-dimensional laser forming, where multiscan is necessary.

Acknowledgment

Support for this project under NSF grant (DMI-0000081) is gratefully acknowledged.

References

[1] Hsiao, Y., et al., 1997, "Finite Element Modeling of Laser Forming," *Proceedings of ICALEO '97*, Section A, pp. 31–40.
[2] Magee, J., et al., 1998, "Advances in Laser Forming," J. Laser Appl., **10**, No. 6, pp. 235–246.
[3] Bao, J., and Yao, Y. L., 1999, "Study of Edge Effects in Laser Bending," *Proc. ASME IMECE 1999, Symposium on Advanced in Metal Forming*, Nashville, TN, Nov., Vol. MED-10, pp. 941–948.
[4] Li, W., and Yao, Y. L., "Convex Laser Forming with High Certainty," Trans. of the North American Manufacturing Research Institution of SME, XXVIII, pp. 33–38.
[5] Li, W., and Yao, Y. L., 2000, "Numerical and Experimental Study of Strain Rate Effects in Laser Forming," ASME J. Manuf. Sci. Eng., **122**, August, pp. 445–451.
[6] Li, W., and Yao, Y. L., 2001, "Laser Bending of Tubes: Mechanism, Analysis and Prediction," ASME J. Manuf. Sci. Eng., **123**, Nov., pp. 674–681.
[7] Ramos, J. A., et al., 1998, "Microstructure of Laser Bent Aluminum Alloy Alcad 2024-T3," *Proceedings of ICALEO'98*, Section E, pp. 178–185.
[8] Maher, W., et al., 1998, "Laser Forming of Titanium and Other Materials Is Useable Within Metallurgical Constraints," *Proceedings of ICALEO'98*, Section E, pp. 121–129.
[9] Li, W., and Yao, Y. L., "Laser Forming With Constant Line Energy," The International Journal of Advanced Manufacturing Technology, **17**, pp. 196–203.
[10] Cheng, J., and Yao, Y. L., 2001, "Cooling Effects in Multiscan Laser Forming," Journal of Manufacturing Processes, **3**, No. 1, pp. 60–72.
[11] Sellars, C. M., 1990, "Modeling Microstructural Development During Hot Rolling," Mater. Sci. Technol., **6**, pp. 1072–1081.
[12] Roberts, W., 1982, "Deformation Processing and Structure," ASM, Materials Science Seminar, Krauss, G., ed, ASM, Metals Park, pp. 109.
[13] Jonas, J. J., et al., 1969, "Strength and Structure Under Hot-Working Conditions," Metall. Rev., pp. 1–24.
[14] Karhausen, K., and Kopp, R., 1992, "Model for Integrated Process and Microstructure Simulation in Hot Forming," Steel Res., **63**, No. 6, pp. 247–256.
[15] Pauskar, P., and Shivpuri, R., 1999, "A Microstructure Dependent Flow Stress Model," Transaction of the North American Manufacturing Research Institute of SME, XXVII, pp. 67–72.
[16] Ashby, M. F., and Easterling, K. E., 1984, "Transformation Hardening of Steel Surfaces by Laser Beams-Part I. Hypo-Eutectoid Steels," Acta Metall., **32**, No. 11, pp. 1935–1948.
[17] Chen, C., et al., 1996, "Eutectoid Temperature of Carbon Steel During Laser Surface Hardening," J. Mater. Res., **11**, No. 2, pp. 458–468.
[18] Shigenobu, N., et al., 1992, "Prediction of Microstructure Distribution in the Through-Thickness Direction During and After Hot Rolling in Carbon Steels," ISIJ Int., **302**, No. 3, pp. 377–386.
[19] Senuma, T., and Yada, H., 1986, "Microstructural Evolution of Plain Carbon Steels in Multiple Hot Working," *Proceedings of the Riso International Symposium on Metallurgy and Materials Science, 7th.*, pp. 547–552.
[20] Anderson, J. G., and Evans, R. W., 1996, "Modeling Flow Stress Evolution

During Elevated Temperature Deformation of Low Carbon Steels,'' Ironmaking Steelmaking **23**, No. 2, pp. 130–135.
[21] Laasraoui, A., and Jonas, J. J., 1991, ''Prediction of Steel Flow Stress at High Temperature and Strain Rates,'' Metall. Trans. A, **22**, pp. 1545–1558.
[22] Hosford, W. F., and Caddel, R. M., 1983, *Metal forming—Mechanics and Metallurgy*, New York, Prentice Hall.
[23] Blum, W., 1982, ''On Modeling Steady State and Transient Deformation at Elevated Temperature,'' Scr. Metall., **16**, pp. 1353–1357.
[24] Koinstinen, D. P., and Marburger, R. E., 1959, ''A General Equation Prescribing the Extent of the Austenite-Martensite Transformation in Pure Iron-Carbon Alloys and Plain Carbon Steels,'' Acta Metall., **7**, pp. 59–60.
[25] Arata, Y., 1981, ''Basic Characteristics of Large Output High Energy Density Heat Source,'' *Proceedings of 1st Joint U.S/Japan Int. Laser Processing Conf., Laser Institute of America*, Toledo, Ohio, Paper. No. 2.
[26] Mazumder, J., 1983, ''Laser Heat Treatment: The State of Art,'' J. Met., **35**, No. 5, pp. 18–26.
[27] Liu, J., 1990, ''The Thermodynamical Study About the Transformation Point of Steel During Laser Transformation Hardening,'' Key Eng. Mater., **46&47**, pp. 153–160.
[28] Boyer, H. E., and Gray, A. G., eds., 1977, *Atlas of Isothermal Transformation and Cooling Transformation Diagrams*, American Society for Metals.